

Multistage modeling of protein dynamics with monomeric Myc oncoprotein as an exampleJiaojiao Liu,^{1,*} Jin Dai,^{1,†} Jianfeng He,^{1,‡} Antti J. Niemi,^{1,2,3,4,5,§} and Nevena Ilieva^{6,||}¹*School of Physics, Beijing Institute of Technology, Beijing 100081, People's Republic of China*²*Nordita, Stockholm University, Roslagstullsbacken 23, SE-106 91 Stockholm, Sweden*³*Department of Physics and Astronomy, Uppsala University, P. O. Box 803, S-75108, Uppsala, Sweden*⁴*Laboratoire de Mathématiques et Physique Théorique CNRS UMR 6083, Fédération Denis Poisson, Université de Tours, Parc de Grandmont, F37200, Tours, France*⁵*Physics of Living Matter, School of Biomedicine, Far Eastern Federal University, Vladivostok 690950, Russia*⁶*Institute of Information and Communication Technologies, Bulgarian Academy of Sciences, 25A, Acad. G. Bonchev Str., Sofia 1113, Bulgaria*

(Received 5 December 2016; published 9 March 2017)

We propose to combine a mean-field approach with all-atom molecular dynamics (MD) into a multistage algorithm that can model protein folding and dynamics over very long time periods yet with atomic-level precision. As an example, we investigate an isolated monomeric Myc oncoprotein that has been implicated in carcinomas including those in colon, breast, and lungs. Under physiological conditions a monomeric Myc is presumed to be an example of intrinsically disordered proteins that pose a serious challenge to existing modeling techniques. We argue that a room-temperature monomeric Myc is in a dynamical state, it oscillates between different conformations that we identify. For this we adopt the C α backbone of Myc in a crystallographic heteromer as an initial ansatz for the monomeric structure. We construct a multisoliton of the pertinent Landau free energy to describe the C α profile with ultrahigh precision. We use Glauber dynamics to resolve how the multisoliton responds to repeated increases and decreases in ambient temperature. We confirm that the initial structure is unstable in isolation. We reveal a highly degenerate ground-state landscape, an attractive set towards which Glauber dynamics converges in the limit of vanishing ambient temperature. We analyze the thermal stability of this Glauber attractor using room-temperature molecular dynamics. We identify and scrutinize a particularly stable subset in which the two helical segments of the original multisoliton align in parallel next to each other. During the MD time evolution of a representative structure from this subset, we observe intermittent quasiparticle oscillations along the C-terminal α helix, some of which resemble a translating Davydov's Amide-I soliton. We propose that the presence of oscillatory motion is in line with the expected intrinsically disordered character of Myc.

DOI: [10.1103/PhysRevE.95.032406](https://doi.org/10.1103/PhysRevE.95.032406)**I. INTRODUCTION**

All-atom molecular dynamics (MD) [1] aims to simulate the time evolution of every single atom in a given protein, including solvents [2]. It produces a discrete and piecewise linear time trajectory of each atom, as a solution of a discretized (semi-)classical Newton's equation. Thus the dimensionless ratio between the iteration time step Δt and the time scale τ of a characteristic atomic motion,

$$e \sim \frac{\Delta t}{\tau}, \quad (1)$$

should be small. Usually τ relates to the frequency of a covalent bond oscillation that has a duration of a few femtoseconds. As a result, Δt should be very short and canonical values are around 1–2 fs. The need for such a short time step makes an all-atom approach to protein dynamics an extreme computational challenge [2–4]. For example, the folding time of a myoglobin is around 2.5 s [5] which can be considered a fairly representative duration in the case of many proteins. At the same time, MD can at best produce around 10 μ s of

in vitro folding trajectory per day *in silico* [6], and this is in the case of proteins which are much shorter than myoglobin. It would probably take close to 1000 years for presently available computers to simulate a single all-atom folding trajectory of myoglobin. Moreover, the currently available all-atom force fields are not perfect [2]. Their limitations tend to essentially affect a folding trajectory no later than around 10 μ s [6]. Coarse-grained techniques are being developed to overcome the bottleneck of short time steps but with loss in accuracy [2,7]; see Ref. [8] for a recent survey of different approaches.

There are many examples in physics where a description in terms of fundamental level constituents is too strenuous. In such cases the concept of a mean-field theory can provide a pragmatic alternative [9]. It has been proposed that a mean-field approach could be introduced to model proteins in terms of the C α backbone [10–18]. For this we note that any biologically relevant time scale is long in comparison to the period of a covalent bond oscillation. Thus the distance between two neighboring C α atoms can be approximated by the average value, which is around 3.8 Å. A Landau free energy then engages only the bond angles $\kappa \in [0, \pi)$ and the torsion angles $\tau \in [-\pi, \pi)$ of the C α skeletal as structural order parameters, as shown in Fig. 1.

Moreover, the bond angles are known to have very small variations along a protein backbone, both in static Protein Data Bank (PDB) [19] structures and during dynamical MD simulations, as confirmed by Figs. 2 and 3.

*ljhappy1207@163.com

†daijing491@gmail.com

‡hjf@bit.edu.cn

§Antti.Niemi@physics.uu.se

||nilieval@mail.cern.ch

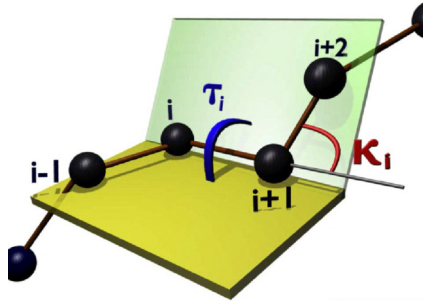


FIG. 1. Definition of bond (κ_i) and torsion (τ_i) angles in relation to the i th $C\alpha$ atom.

Thus, the relative difference in values of κ_i between two neighboring residues

$$\Delta\kappa_i = \frac{|\kappa_{i+1} - \kappa_i|}{\pi} \quad (2)$$

is small and can be employed as an expansion parameter in lieu of (1). In particular, since an expansion in (2) does not relate to any time scale, a mean-field description can at least in principle describe time trajectories over any time period.

Here we propose to combine mean-field theory with all atom molecular dynamics into a multistage algorithm to model protein dynamics, and in particular intrinsically unstructured proteins, over long time periods yet with atomic level scrutiny. We use mean-field theory to leap over high energy barriers and long time periods. We refine the structure to the atomic level by following how it evolves over a short time period using all-atom MD. The algorithm goes as follows. We first construct the Landau free energy that models a given protein structure. The initial ansatz can either be taken from PDB, or it can be constructed using homology modeling with all-atom MD refinement as in Ref. [6]. We then proceed to locate the minimum energy configurations of the Landau free energy. For this we use the Glauber algorithm [21,22] to repeatedly increase and decrease the ambient temperature between very high and very low values. In the limit of very low temperatures, at the end of heating and cooling, the structure settles near a local minimum of the free energy. Thus, by numerously repeating a heating and cooling cycle, we can reveal the low-energy landscape, as the set of structures towards which

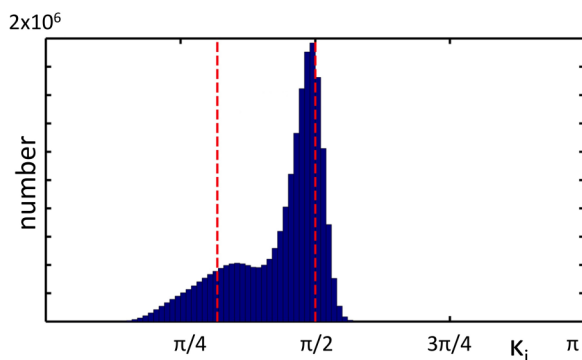


FIG. 2. Distribution of bond angles κ in crystallographic PDB structures. Note that for α helices $\kappa \approx \pi/2$ and for β strands $\kappa \approx 1$.

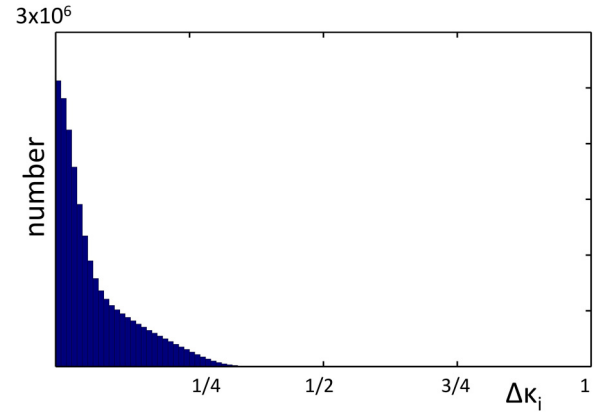


FIG. 3. The distribution of values (2) along the $C\alpha$ backbone during the Villin simulation in Anton [20]. Based on data obtained from authors.

the $C\alpha$ backbone becomes attracted in the low-temperature limit of the Glauber algorithm. Once we have found such a Glauber attractor of low-energy structures, we proceed to refine and scrutinize it using all-atom MD. When certain predetermined convergence and stability criteria are met, the simulation is considered complete and the algorithm is terminated. Otherwise, the procedure is repeated.

As an example, we investigate the topography of Glauber attractor in the case of the biomedically highly important Myc proto-oncogene protein [23–29]. Malfunctioning and overexpression of Myc has been implicated in a number of human cancers, from lymphomas and leukemias to carcinomas in colon, breast, and lungs. Thus, Myc is considered a promising target for cancer therapeutics and development of anticancer drugs. Under physiological conditions a monomeric Myc is presumed to be intrinsically unstructured and it is not known to have any direct biological effect. Apparently, Myc becomes functionally active only when it stabilizes into a DNA binding basic-helix-loop-helix-leucine-zipper conformation on heterodimerization with Max; see Fig. 4.

As a component of the heterodimer, Myc then participates in processes such as cell cycle progression, apoptosis, and cellular transformation by regulating the transcription of the relevant target gene.

We analyze a monomeric Myc in isolation, as a biomedically important exemplar to develop our methodology: There should be a correlation between the conformation of a monomeric Myc and the rate at which it can heterodimerize with Max *in vivo*. We start our analysis from a crystallographic structure of the Myc-Max heteromer which is bound to DNA;

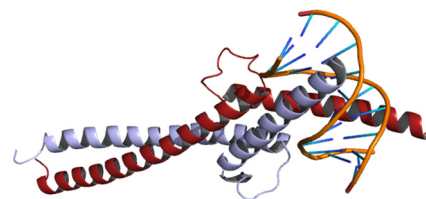


FIG. 4. The $C\alpha$ backbone of the crystallographic PDB structure INKP, with a segment of DNA. Myc in red and Max in blue.

we use the structure with PDB code 1NKP [28], which is shown in Fig. 4. We construct the initial Landau free-energy ansatz of monomeric Myc using the conformation it has in the heterodimer. We subject the Landau model of Myc to repeated heating and cooling cycles using the Glauber algorithm. We categorize the $C\alpha$ structures towards which it becomes attracted on cooling. We observe that the resulting Glauber attractor accumulates along a linear trajectory in terms of root-mean-square distance (RMSD) and radius of gyration R_g . This trajectory emanates from the initial Myc structure and proceeds towards decreasing R_g , and energy. We identify five different structural clusters along the mean-field trajectory, and we select a representative from each cluster for MD simulation stability analysis. We use molecular dynamics package GROMACS 4.6.3 [30] with the united-atom force field GROMOS53a6, which we have previously analyzed and compared with all-atom force fields CHARMM27 and OPLS/AA [31] in a closely related context; we deduce that GROMOS53a6 is the most reliable among the three force fields for the present purposes. We perform the MD simulation near room temperature at 290 K and we limit the simulation duration to 50 ns *in vitro*: Since we are interested in the local stability and refinement of the initial structure, we do not attempt a full-scale all-atom MD search of a folded Myc. Besides, we doubt that any presently available computer power is sufficient for such an analysis. We find that in four of the clusters we identify, the MD trajectory drifts away from the cluster. Accordingly, these clusters are unstable under MD time evolution. However, the fifth cluster is remarkably stable under MD evolution. The MD simulation is only slightly readjusting the positioning of the backbone and side-chain atoms. But during the MD evolution of the representative that we have chosen from the apparently stable cluster, we also observe intermittent oscillatory behavior, some aspects of which resemble a propagating, asymmetric Amide-I *Davydov soliton* [32,33].

Our Glauber dynamics simulations are swift. A full heating and cooling cycle takes only around 1 min *in silico*, when we use a single processor in a current Apple Pro desktop computer. The MD analysis is much more tedious: The ideal length of a MD trajectory seems to be around a few microseconds [6]. However, the computer resources that are available to us in practice limit the duration of our MD trajectories to around 100 ns. Moreover, we do not repeat our multiscale algorithm beyond its first level of iteration. Since we identify an apparently MD stable assembly already after a single iteration, the example we present serves as a proof-of-concept exercise. For a firmer conclusion on Myc and its landscape of assemblies, the technology described in Ref. [6] should be used.

II. METHODS

A. Mean-field theory

A mean-field model of a protein is built as follows: Most biologically relevant processes have a time scale which is very long in comparison to the period of a covalent bond oscillation. Thus, over any biologically relevant time period we can approximate the distance between two neighboring $C\alpha$ atoms with the average value 3.8 Å of a crystallographic PDB

structure. The skeletal $C\alpha$ bond κ and torsion τ angles that we define in Fig. 1 then constitute a complete set of structural order parameters. As shown in Figs. 2 and 3, the bond angles are relatively rigid and slowly varying; the differences $\Delta\kappa_i$ in (2) are small. Thus, the Landau free energy $E(\kappa, \tau)$ can be expanded in powers of these differences. A detailed analysis in Refs. [10–18] shows that in the limit of small $\Delta\kappa_i$ the free energy admits the following expansion:

$$E(\kappa, \tau) = \sum_{i=1}^{N-1} \Delta\kappa_i^2 + \sum_{i=1}^N \left\{ \lambda (\kappa_i^2 - m^2)^2 + \frac{d}{2} \kappa_i^2 \tau_i^2 - b\kappa_i^2 \tau_i - a\tau_i + \frac{c}{2} \tau_i^2 \right\} + \mathcal{O}(\Delta\kappa_i^4). \quad (3)$$

Here (λ, m, a, b, c, d) are parameters. For a given PDB protein structure these parameters are determined by training a minimum energy configuration of (3) to model the PDB backbone. There is a program PROPRO that can be used to train the parameters in (3) so the model describes a given PDB structure. The program can be used online [34].

We recognize in (3) a modification of the Hamiltonian that defines the discrete nonlinear Schrödinger (DNLS) equation [11,12]. The first row coincides with a *naive* discretization of the continuum nonlinear Schrödinger equation. The fourth term (b) is the conserved momentum in the DNLS model, the fifth (a) term is the Chern-Simons term, and the sixth (c) term is the Proca mass. Note that both momentum and Chern-Simons are chiral. We refer to Refs. [35,36] for detailed analyses.

B. Validation of mean-field approach

In the case of proteins we validate (3) qualitatively with the following line of arguments: According to Refs. [37–39], the folding of a protein is a “cooperative” process that resembles a first-order phase transition. Indeed, the DNLS equation supports solitons which are the paradigm cooperative organizers in numerous physical scenarios. A soliton emerges as a solution of the variational equations that coincide with the extrema of (3). For this we first eliminate the torsion angles using the equation

$$\tau_i[\kappa] = \frac{a + b\kappa_i^2}{c + d\kappa_i^2}. \quad (4)$$

For bond angles we then obtain

$$\kappa_{i+1} = 2\kappa_i - \kappa_{i-1} + \frac{dV[\kappa]}{d\kappa_i^2}, \quad (5)$$

where

$$V[\kappa] = -\left(\frac{bc - ad}{d}\right) \frac{1}{c + d\kappa^2} - \left(\frac{b^2 + 8\lambda m^2}{2b}\right) \kappa^2 + \lambda \kappa^4.$$

The difference equation (5) can be solved iteratively, for example, using the algorithm in Refs. [12]; a soliton solution models a supersecondary protein structure such as a helix-loop-helix motif and the loop corresponds to the soliton proper. The parameter m is the main regulator of the secondary structure, and its value specifies whether we have an α helix, a β strand, or some other kind of regular pattern. Details can be found in Refs. [10–18].

In order to reveal a relation between (3) and the structure of a first-order phase transition, we note that in the case of a protein the bond angles are rigid and the torsion angles are flexible. In particular, the variations of κ_i along the backbone are small and cover only a portion of the allowable range of κ as shown in Figs. 2 and 3. Thus, over sufficiently large distance scales we may try and proceed self-consistently to ignore fluctuations and use the mean value $\kappa_i \sim \kappa$. We can then solve for this mean value κ in terms of the mean value of torsion angles $\tau_i \sim \tau$. From (3)

$$\frac{\delta E}{\delta \kappa} = 0 \Rightarrow \kappa^2 = m^2 + \frac{b}{2\lambda}\tau - \frac{d}{4\lambda}\tau^2. \quad (6)$$

We substitute this into the equation that determines the extrema of (3) with respect to variations in τ ,

$$\begin{aligned} \frac{\delta E}{\delta \tau} = 0 \Rightarrow \\ \frac{d^2}{4\lambda}\tau^3 - \frac{3bd}{4\lambda}\tau^2 + \left(\frac{b^2}{2\lambda} - dm^2 - c\right)\tau + (a + bm^2) = 0. \end{aligned} \quad (7)$$

This equation coincides with the variational equation that specifies the extrema of the following free energy:

$$\frac{d^2}{16\lambda}\tau^4 - \frac{db}{4\lambda}\tau^3 + \left(\frac{b^2}{4\lambda} - \frac{dm^2}{2} - \frac{c}{2}\right)\tau^2 + (a + bm^2)\tau. \quad (8)$$

This has the canonical form of the Landau–De Gennes free energy for a first-order phase transition [40], thus completing a *naive* qualitative validation of (3) along the arguments in [37–39].

C. Long-distance interactions in mean-field theory

A protein chain is subject to long-distance interactions which in a MD approach are modeled by a hydrogen bond or Lennart-Jones, Coulomb, and other force fields. In the present mean-field theory these interactions are presumed to be taken into account through the nonlinear terms in the free energy, except for the short-distance Pauli repulsion which needs to be introduced explicitly. In the leading order it suffices to proceed as follows: A statistical analysis of PDB structures shows that two $C\alpha$ atoms located at sites i and k respectively that are *not* nearest neighbors along the backbone obey the constraint

$$|\mathbf{r}_i - \mathbf{r}_k| > 3.8 \text{ \AA} \quad \text{for } |i - k| \geq 2. \quad (9)$$

We impose this constraint as a rigid acceptance criterion in the Monte Carlo algorithm. More elaborate forms of short- and long-distance interactions could also be introduced, and we refer to Ref. [41] for analysis.

D. Glauber algorithm and fluctuations in mean-field approach

Arrhenius's law states that the reaction rate r depends exponentially on the ratio of activation energy H and the physical temperature factor $k_B\theta$,

$$r \propto \exp\left\{-\frac{H}{k_B\theta}\right\}.$$

Here k_B the Boltzmann constant and θ is the temperature measured in kelvin. On the other hand, Glauber dynamics

assumes that the transition probability from a state a to another state b has the form

$$\mathcal{P}(a \rightarrow b) = \frac{1}{1 + e^{\Delta E_{ba}/T}}, \quad (10)$$

where $\Delta E_{ba} = E_b - E_a$ is the activation energy, and in the mean-field approach we compute it from (3). The parameter T is the Monte Carlo temperature factor. In general it does not coincide with the physical temperature factor $k_B\theta$, but the two can be related by methods of renormalization group [42]; here we do not need an explicit relation, ultimately the molecular dynamics step in our algorithm will determine the temperature.

A small two-state protein often folds in line with Arrhenius's law [43], and for a simple spin chain the Glauber algorithm reproduces Arrhenius law. Furthermore, a protein backbone with its side chains has a structure that resembles a spin chain [15]. Thus we proceed by assuming that Glauber dynamics is a good leading-order approximation to model aspects of protein dynamics.

E. Side chains in a mean-field approach

The mean-field theory (3) builds on the $C\alpha$ coordinates. There is no direct information on the side-chain coordinates, and their effects are accounted for implicitly by the interactions in (3). Once we have found a minimal energy $C\alpha$ structure, we can reconstruct an ansatz for the all-atom structure using side-chain libraries; here we use *Pulchra* [44]. We can then employ MD to refine the ensuing side-chain structure if need be [6]. Accordingly, we proceed as follows: Once we have constructed a set of minimal energy $C\alpha$ structures using Glauber dynamics, we screen it using *Pulchra* and proceed only with those $C\alpha$ structures that are void of all-atom steric clashes. For this we demand that the distance between any pair of atoms that are *not* covalently bonded is larger than a predetermined cut-off distance R_0 . The covalent bond distance among C, N, and O atoms is at most around $\sim 1.54 \text{ \AA}$, and thus we adopt the following global value:

$$R_0 = 1.6 \text{ \AA}. \quad (11)$$

We only proceed to our MD stability analysis with such mean-field structures that pass this screening.

F. Molecular dynamics

We use the molecular dynamics package GROMACS 4.6.3 [30]. We analyze in detail 50-ns-long trajectories, with initial configurations that we specify in the sequel. We use the Gromos53a6 force field, with a time step of 2 fs. We motivate our choice of force field by the analysis in Ref. [31]. We use periodic boundary conditions, with 0.9-nm cutoff for long-distance interactions. The box is rectangular, with a distance of 2.0 nm between the protein and the box walls; we adjust the box size depending on the initial configuration. We use a salt concentration of 0.15 mol/l and temperature 290 K, supported with a Berendsen thermostat in the equilibration phase and with a v-rescale thermostat in the production run. The pressure is kept constant with the Berendsen barostat and changed to Parrinello-Rahman in the production run. The changes ensure that we generate a proper canonical ensemble.

TABLE I. Structure assignment of Myc in PDB entry 1NKP chain A.

Structure	Residues	Number of residues
Base	GLY897-ARG914	18
Helix	ASN915-ILE928	14
Loop	PRO929-PRO938	10
Helix	LYS939-CYS984	46

We record the coordinates every 2 ps, which gives us 2500 frames for each production run.

III. RESULTS

A. Myc as a multisoliton

Our starting point is the crystallographic PDB structure with code 1NKP [28] shown in Fig. 4. It describes a DNA-bound heterodimer of Myc and Max in a base-helix-loop-helix leucine zipper conformation, with 1.8 Å resolution. We use chain A where the sites with PDB index 897-984 correspond to Myc, and its major features are summarized in Table I.

In Figs. 5 (top) and 5 (bottom), we show the bond and torsion angles of Myc in 1NKP, respectively. In these figures we follow Ref. [45] and extend the range of bond angle into $\kappa \in [-\pi, \pi)$. Thus there is a twofold covering of the geometry by the bond angles, which we compensate for with a discrete local \mathbb{Z}_2 symmetry. We employ this symmetry to identify the

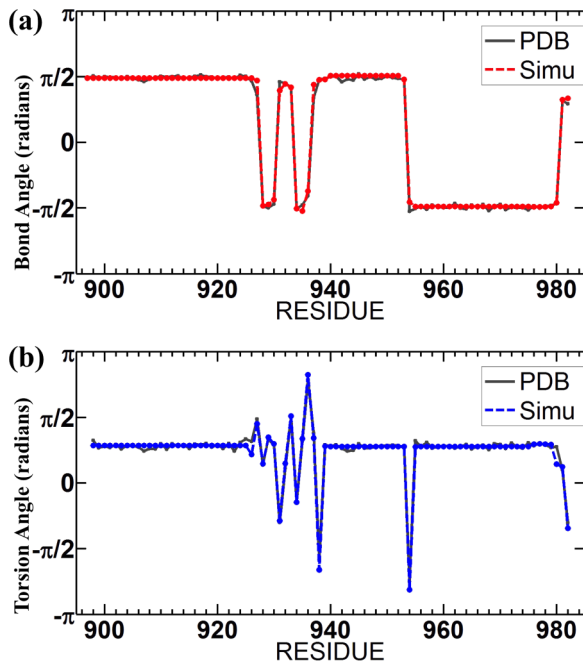


FIG. 5. (a) The bond κ angle spectrum of 1NKP after we introduce the \mathbb{Z}_2 transformation that identifies the soliton structure (gray), together with the corresponding spectrum of the multisoliton structure (red). (b) The torsion τ angle spectrum of 1NKP after the \mathbb{Z}_2 transformation that identifies the soliton structure in top figure (gray) together with the corresponding spectrum of the multisoliton structure (blue).

TABLE II. Parameters for each soliton.

Parameter	Soliton-1	Soliton-2	Soliton-3
b	8.731 e-11	1.588 e-8	6.486 e-10
d	1.268 e-7	7.637 e-8	5.832 e-8
e	1.004 e-11	8.77 e-10	1.888 e-10
q	-5.944 e-8	-6.827 e-7	-5.755 e-9
c1	5.459	2.603	4.459
c2	2.318	2.252	4.13
l	1.539	1.494	1.405
m2	1.651	1.404	1.655
Parameter	Soliton-4	Soliton-5	Soliton-6
b	3.414 e-10	4.4967 e-9	1.148 e-9
d	4.865 e-8	6.943 e-10	3.402 e-8
e	1.501 e-10	7.612 e-15	1.353 e-10
q	-5.331 e-8	-2.906 e-7	-7.716 e-8
c1	0.887	3.225	2.872
c2	2.449	2.995	18.223
m1	1.533	1.595	1.54
m2	1.5	1.54	1.049

soliton content, which is visible in Fig. 5 (top): We identify six different individual solitons. Four of the solitons form the loop region of Myc. There is one soliton along the leucine zipper at the location of the turn around residue 954 where we observe a jump in the torsion angle in Fig. 5. There is one soliton at the C terminal of Myc.

In Fig. 5 we also compare the bond and torsion angle values between Myc in 1NKP and its multisoliton. We use the program PROPRO [34] to construct the multisoliton profile, and the parameter values that we find for the Landau free energy are given in Table II; we have rounded the numbers to four digits, and higher precision is easily obtained using Ref. [34].

In Fig. 6 we interlace the original PDB structure of Myc with the multisoliton profile. The RMSD between the two is 0.98 Å.

In Fig. 7 we compare the residue-wise distance of the $C\alpha$ atoms in the multisoliton from those in the crystallographic structure. We also show an estimate of the one-standard-deviation error in the crystallographic coordinates, which we compute from the B factors using the Debye-Waller relation.

B. Glauber attractor and minima of Landau free energy

We subject the multisoliton to successive heating and cooling simulations using the Glauber algorithm. Our goal is to identify the low-temperature Glauber attractor. This we define as the set of all the structures towards which the



FIG. 6. Comparison between the crystallographic Myc (gray) and its multisoliton (red).

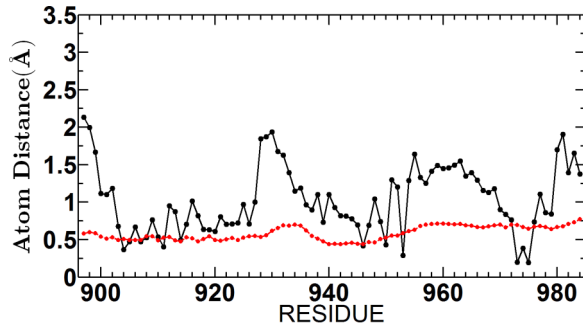


FIG. 7. Residue-wise distance of the $C\alpha$ atoms in the multisoliton from their crystallographic coordinates. The red line shows the Debye-Waller one- σ fluctuation distance in the PDB structure.

Glauber algorithm converges in the limit of vanishing ambient temperature. *A priori*, the Glauber attractor should coincide with the landscape of local minima of the Landau free energy.

As we increase the ambient temperature, the multisoliton structure starts to thermally fluctuate. At sufficiently high temperatures the structure can cross over energy barriers that surround the initial multisoliton profile. If the multisoliton is not stable, then the structure can be expected to start drifting away from its vicinity. When the ambient temperature subsequently decreases, the structure becomes attracted towards a local minimum of the free energy. In the case of a protein such as myoglobin that has an essentially unique and stable fold, the final conformation coincides with the initial multisoliton. However, if the protein is intrinsically unstructured there are in general several local minima and/or high levels of degeneracy in the free-energy landscape to which it can become attracted; the final conformation does not need to be unique. In fact, it can differ considerably from the initial one. The Glauber attractor can have an elaborated topography. When we repeat the heating and cooling cycle sufficiently many times, with sufficiently high-temperature variations, we expect to eventually resolve for the Glauber attractor.

In the case of Myc we deduce that $T_H = 10^{-9}$ and $T_L = 10^{-14}$ can be considered representative for the high- and low-temperature factor values that we use in the Glauber algorithm (10). Similarly, we conclude that 50×10^6 is a representative number of Monte Carlo steps for a heating and cooling cycle. In a single cycle we first take 5×10^6 steps at the low-temperature factor value T_L to fully thermalize the system. We then increase T during 10×10^6 steps linearly on a logarithmic temperature scale, to the high-temperature factor value T_H , and thermalize the system at T_H during 20×10^6 steps. We conclude the cycle by lowering T back to T_L by reversing the heating process. We repeat the cycle until we are confident that we have identified the Glauber attractor. We have performed several repeated heating and cooling simulations, with the number of cycles varying between 2500 and 5000. Accordingly, we have very good statistics. There are two production runs that we analyze in detail. In one we use the full-length Myc structure while in the other we exclude the residues near the flexible N and C terminals and simulate only the segment between amino acids 901 and 979. We find the same Glauber attractor in both cases. We always perform all MD simulations with the full chain length.

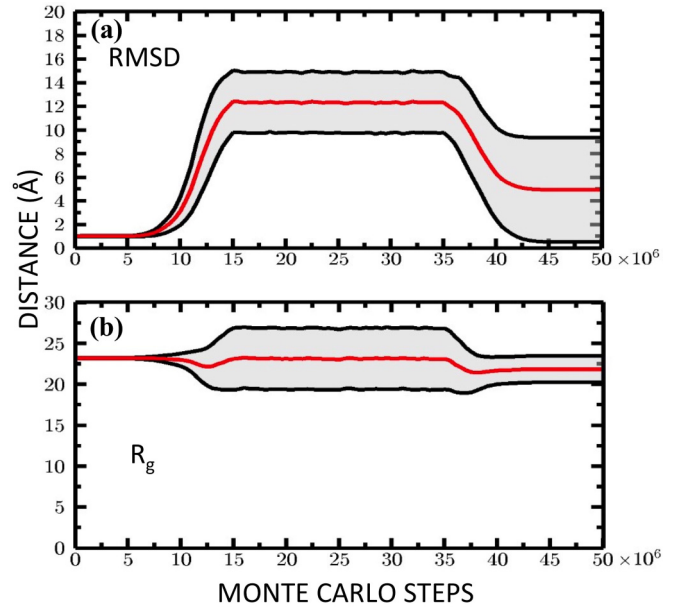


FIG. 8. (a) Evolution of RMSD distance from the crystallographic Myc structure during the heating and cooling cycle. (b) Evolution of radius of gyration R_g during the heating and cooling cycle. The red line denotes the average value over 5175 simulations, and the gray band determines the one- σ deviation from the average value.

Figure 8 shows the statistical evolution of RMSD and the radius of gyration R_g that we obtain in all our heating and cooling cycles.

There is, on average, an approximately 5 Å RMSD distance between the initial crystallographic structure and the final structure. This distance is larger than the ~ 4.2 Å one-standard-deviation spread that we observe in the average value of the RMSD distance from the crystallographic Myc. Thus the Glauber attractor is degenerate, and there does not appear to be a single folded state. In particular, the initial multisoliton is not stable. Such a degeneracy can be expected in the case of an intrinsically unstructured protein.

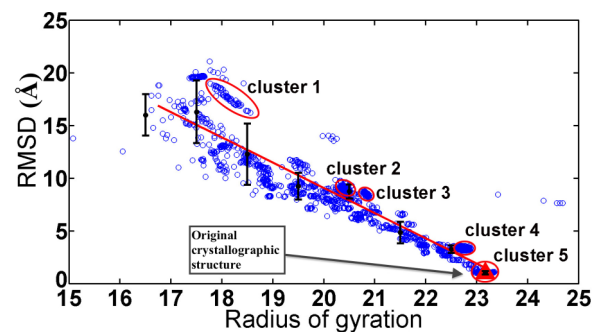


FIG. 9. The low-temperature Glauber attractor on the R_g vs. RMSD plane. The five different clusters that we have analyzed in detail are identified. The initial multisoliton is marked with a red triangle in cluster 5. The error bars denote a one-standard-deviation distance around the average value that determines the average line (12).

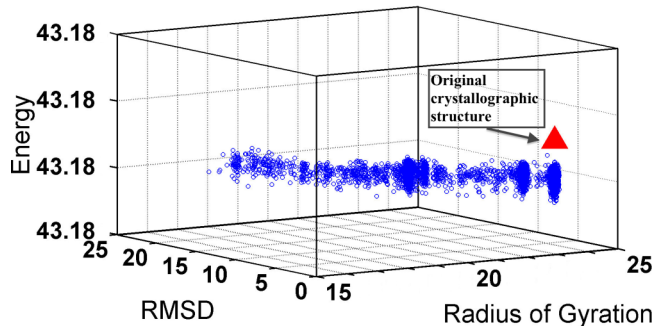


FIG. 10. (Top) The energy landscape of the Glauber attractor, in terms of R_g vs. RMSD of the final structures. The multisoliton is marked with a red triangle. Note that the energy of the attractor is highly degenerate, and free-energy differences are minor. The RMSD and radius of gyration are measured in Ångströms, and the energy unit is defined by the overall normalization of (3).

In Fig. 9 we present the Glauber attractor on the RMSD vs. R_g plane. The figure reveals a highly degenerate landscape of ground-state conformations. We observe an apparent tendency for the ground-state conformations to form disjoint clusters. In the figure we have identified five clusters as examples that we have analyzed in more detail. Note that one of these examples (cluster number 5) corresponds to structures that return to the vicinity of the initial multisoliton of the crystallographic Myc. We observe that the full Glauber attractor is tightly located around the line

$$\text{RMSD} \approx -2.4 R_g + 56.9 \quad (\text{Å}). \quad (12)$$

Figure 9 shows that the initial multisoliton has a tendency to collapse towards spatially more compact structures.

Figure 10 shows the Landau free-energy landscape of a Glauber attractor as a function of R_g and RMSD.

The initial multisoliton is marked by a red triangle. It is unstable, and its Landau free energy is above that of Glauber attractor states. We note that the free energy is highly degenerate, to the extent that the clusters of Fig. 9 appear as space-filling point sets, prolated along the energy axis on the scale that we use in the figure. A space-filling ground-state degeneracy is in line with the expected intrinsically unstructured character of Myc. Thermal fluctuations move the structure around, making it hop between the different low-temperature states near the local energy minima.

In Table III we summarize the main characteristics of the clusters that we identify in Figs. 9 and 10.

TABLE III. Minimum and maximum RMSD distance of each cluster from the initial Myc structure in INKP.

Cluster	min	max
1	16.2	18.7
2	8.7	9.2
3	8.3	8.8
4	3.1	3.4
5	0.9	1.2

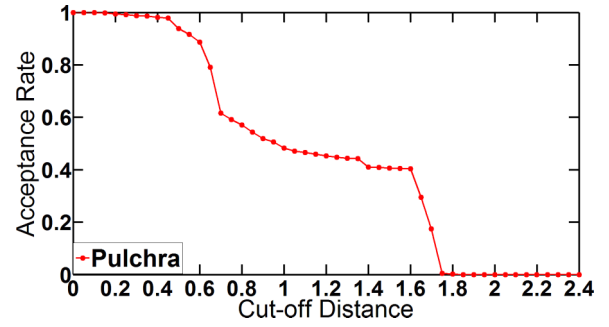


FIG. 11. The fraction of structures in the Glauber attractor with not a single all-atom steric clash according to *Pulchra*, as a function of the cut-off parameter R_0 . Here we adopt the cut-off value $R_0 = 1.6$ Å.

C. Molecular dynamics analysis

We use MD to analyze the *local* spatial and temporal stability of clusters in the Glauber attractor. We perform the simulations at relatively low temperatures, near a room-temperature value 290 K. Higher temperatures entail larger amplitude thermal fluctuations and it becomes difficult to deduce the level of local cluster stability in the background of large-amplitude thermal motions.

The Landau free energy engages only the $C\alpha$ backbone, and thus it can support backbone structures with steric clashes in all-atom structures. We start by screening out such structures that lead to steric clashes. For this we use a *Pulchra* side-chain reconstruction algorithm to recover an all-atom structure from the $C\alpha$ trace. We impose *stringently* the acceptance criterion (11). Figure 11 shows the overall acceptance ratio of

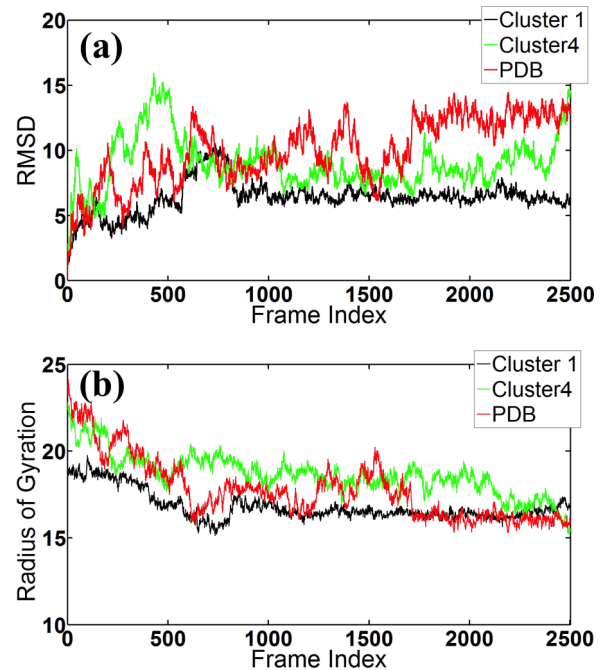


FIG. 12. (a) The evolution of RMSD in the three clusters 1 and 4 and the PDB structure 5 under our MD simulations. (b) The evolution of R_g in the three clusters 1, 4, and 5 under our MD simulations. The RMSD is computed from the initial structure of the simulation, chosen randomly in clusters 1 and 4 and as the multisoliton in cluster 5.

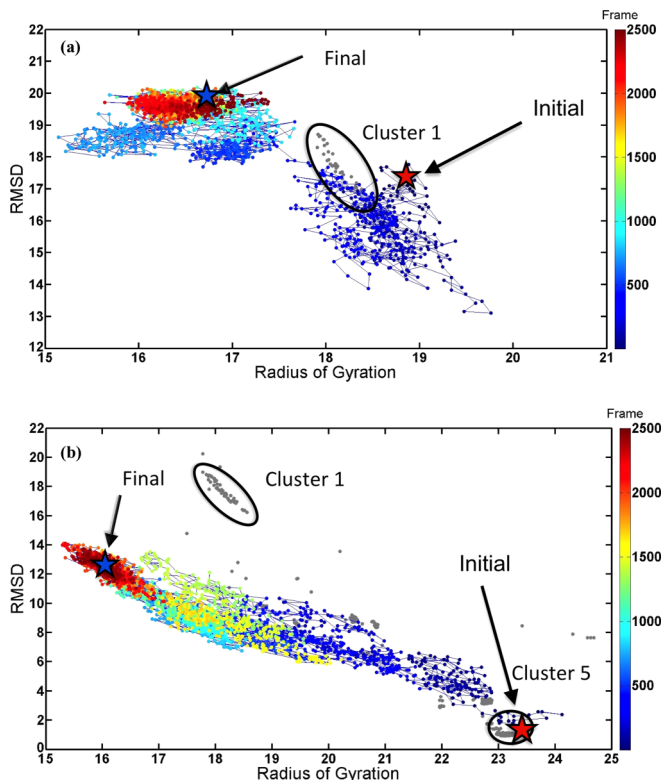


FIG. 13. (a) The evolution of cluster 1 under MD simulation. (b) The evolution of cluster 5 (PDB structure) under MD simulation. Color coding for time evolution is same in both figures, but note the difference in scales.

mean-field $C\alpha$ structures as a function of the cut-off parameter R_0 .

At the value (11) of R_0 around 40 percent of *Pulchra*, structures are sterically fully consistent. In particular, each of the five clusters have representatives with sterically acceptable all-atom structures. But we note a sharp drop in the number of accepted structures when R_0 increases beyond the value (11).

We (randomly) select one all-atom structure from each of the five clusters for MD stability analysis. We find that only cluster 1 appears MD stable. In all other clusters, the initial structure drifts systematically away from the cluster under MD time evolution. We describe the examples in clusters 1, 4, and 5 in more detail: In Fig. 12 (top) we show the evolution of RMSD and in Fig. 12 (bottom) we show the evolution of R_g during our MD simulations.

We note how in both clusters 4 and 5 the initial structure drifts away from the cluster. In cluster 1 the structure also initially moves away, but then the values of RMSD and R_g quickly stabilize: Qualitatively, the evolution in cluster 1 differs from the other two. There is an apparent initial relaxation of the tension in the *Pulchra* side-chain assignment, with corresponding adjustment of the backbone during the first ~ 15 ns. This is followed by a stabilization. In Fig. 13 we compare the evolution trajectory for cluster 1, with cluster 5 of the PDB structure. Cluster 1 converges towards a region which is close to the original cluster, while cluster 5 systematically drifts away from the initial position. The MD trajectories of clusters 1 and 5 differ considerably.

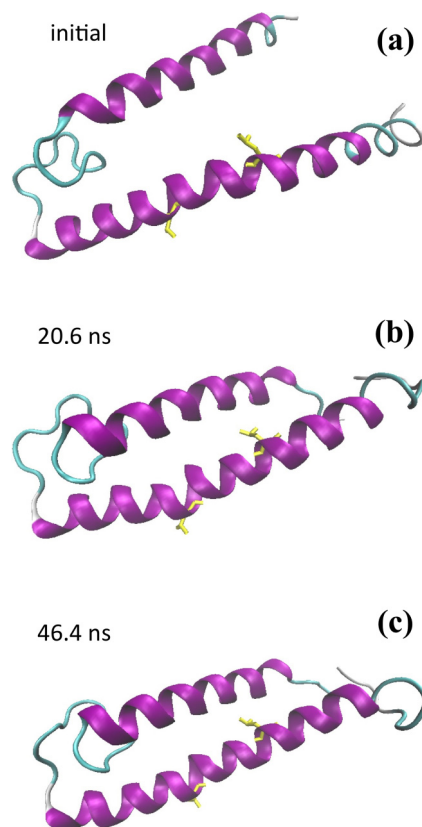


FIG. 14. (a) The initial structure from cluster 1 in the all-atom MD simulation. (b) Representative snapshot structure from halfway around the trajectory. (c) Representative snapshot structure near the end of the MD simulation. In the figures we have identified two residues, Leu-951 and Leu 960.

D. Myc at room temperature

The mean-field structures in cluster 1 have the shape of a hairpin. In Fig. 14 (top) we show a generic structure, the one that we use as the initial configuration in our MD simulation. The two α -helical segments of Fig. 6 have become almost parallel and quite close to each other.

In the course of the MD time evolution the hairpin continues to emerge but intermittently: The hairpin shown in Figs. 14 (middle) and 14 (bottom) repeats itself several times during the time evolution; the middle figure is taken near the halfway point of the MD simulation and the bottom figure is taken close to its end. The two hairpins are almost identical and very similar to the (generic) mean-field cluster 1 structure that we show in the top figure.

Besides the hairpin of Fig. 14, we identify another structure that appears repeatedly in our MD simulation. We show it both in the top (9.74 ns) and bottom (18.52 ns) snapshots of the motion we outline in Fig. 15. This structure is essentially the hairpin of Fig. 14, but with a turn near the middle of one of the two parallel helices. The turn is located right after Leu-951 in the proximity of the turn that we observed previously in the crystallographic structure; see Fig. 5.

We deduce that the MD trajectory is akin to a dynamical two-state system, with oscillatory motion between the hairpin structure of Fig. 14 and the turn-in-helix hairpin structure that we show in the top and bottom snapshots of Fig. 15.



FIG. 15. The MD evolution of the $C\alpha$ backbone between frames 443 and 786 of Fig. 13.

In Fig. 16 we confirm this; in this figure we show the results from a secondary structure analysis of the entire MD trajectory, starting from cluster 1. The secondary structure profile is remarkably stable, except for the oscillatory two-state dynamics between the hairpin of Fig. 14 and the hairpin with

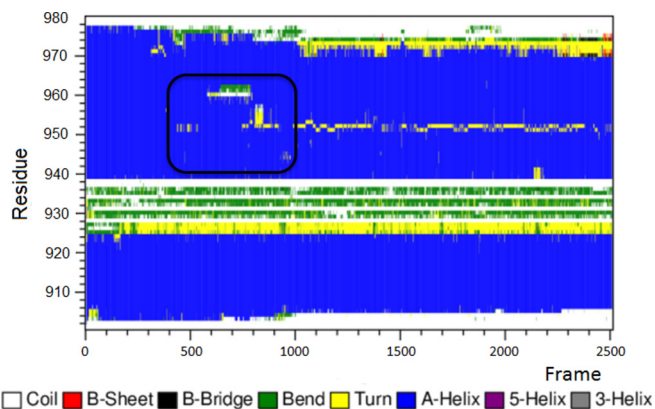


FIG. 16. The do.dssp secondary structure analysis of the MD trajectory. The apparent Davydov soliton in Fig. 15 is identified.

turn-in-helix. The oscillations between the two states start after an initial hairpin stabilization period of around 8 ns.

In Fig. 17 (top) we show the evolution of an angle which is formed between the vector pointing from the $C\alpha$ to $C\beta$ at site Leu-951 and the corresponding vector at site Ala-955. The dynamical two-state oscillatory character of the trajectory is apparent in this figure: After the initial stabilization, the angle between the two vectors jumps between two different values, corresponding to the helix and to the turn-in-helix structures. Such oscillatory behavior between multiple different, energetically degenerate structures has been previously

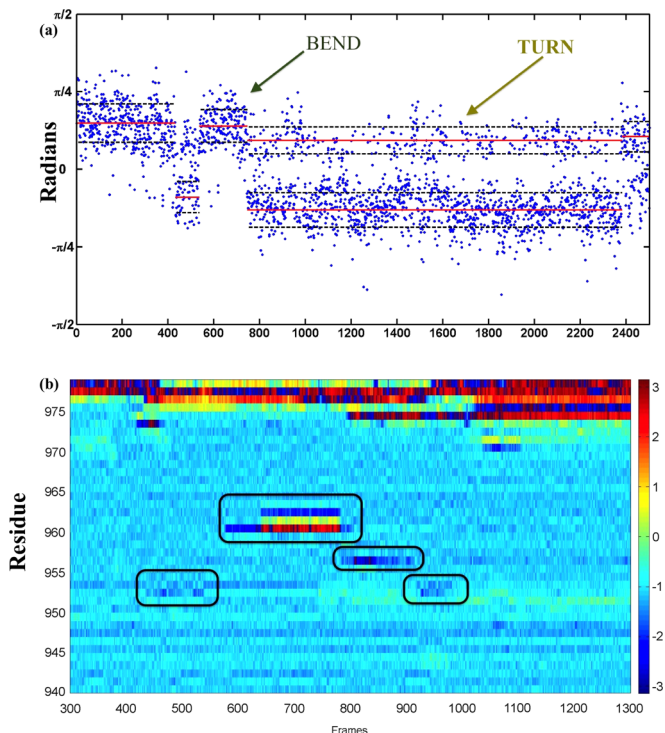


FIG. 17. (a) The angle between vector pointing from $C\alpha$ to $C\beta$ at Leu-951, and the vector pointing from $C\alpha$ to $C\beta$ at Ala-955. (b) The values of the side-chain η angle [31] during frames 200–1300 of the MD simulation of cluster 1. We have encircled the portion that relates to the event in Fig. 15, also identified in Fig. 16.

identified in the case of intrinsically unstructured proteins [46]. Energy degeneracy with several different conformational states, separated by small energy barriers, appears to be symptomatic for these proteins.

In Fig. 17 (bottom) we show the evolution of the side-chain η angles along the entire chain during the MD time evolution. The concept of the η angle has been introduced and analyzed in Ref. [31]. The angle measures difference in the direction between neighboring $C\alpha$ - $C\beta$ vectors, and it characterizes the local twisting of the side-chain assignment along the backbone. The focus in the figure is in the time period between frames 200 and 1300, corresponding to time segment 4.0–26.0 ns. In the figure we identify one relatively long-lived bend intermediate, with the bend located near Leu-960. This intermediate originates from the turn at Leu-951, and we summarize its emergence and evolution in Figs. 15; see also Fig. 16 and Fig. 17 (top) where the intermediate is identified. The bend formation starts with the turn first appearing near Leu-951, as shown in the 9.74-ns snapshot of Fig. 15. This turn propagates to the vicinity of Leu-960, as shown in snapshots at 10.78 ns and 11.58 ns. It stays there as a bend (according to `do.dssp`) for several nanoseconds and then translates back towards Leu-951 (snapshot at 15.98 ns), where it stops and forms a turn (according to `do.dssp`) as shown in the snapshot at 18.52 ns. Finally, the turn dissolves and the structure returns to the hairpin conformation of Fig. 14. The entire oscillatory event lasts around 9 ns, and it is clearly identifiable in our simulations.

We propose that the event we summarize in Figs 15 and 17 (bottom) corresponds to a formation and propagation of Davydov's Amide-I soliton along the α helix: Apparently, the hydrogen bonds that stabilize the α helix occasionally break, causing the formation of a turn near Leu-951. This turn is a localized quasiparticle akin to Davydov's soliton. It propagates along the backbone to the vicinity of Leu-960, bounces back, and returns to Leu-951, where localizes and then dissolves.

IV. SUMMARY

We have proposed to combine an effective mean-field description with molecular dynamics. The outcome is a multiscale algorithm that can be used to model protein

dynamics efficiently both over long time periods and with atomic-level precision. We have applied the algorithm to study properties of Myc, which is a biomedically highly relevant oncoprotein. Myc has an important role in regulation of gene expression, and a malfunctioning or overexpressed Myc has been implicated in many cancers from Burkitt's lymphoma and neuroblastomas to carcinomas of colon, breast, and lungs. Accordingly, Myc is subject to vigorous pharmaceutical and biomedical research, and it is a potentially highly important target to anticancer drugs.

An isolated monomeric Myc is presumed to be intrinsically unstructured under physiological conditions. Moreover, as a monomer Myc has no known biological function, it becomes biological active only in a heterodimer with protein Max. The heteromerization rate of Myc and Max should depend on the conformational state of an isolated monomeric Myc *in vivo*. Thus, the investigation of the conformational landscape in the case of an isolated Myc should have direct biomedical relevance: When we understand the physical properties of a monomeric Myc, we can identify mechanisms to control the rate at which Myc and Max heterodimerize.

We have found that at room temperature a monomeric Myc has a tendency to turn into a hairpinlike conformation. We have also found that this conformation is unstable. It tends to occasionally buckle, at a specific location that we have identified. Moreover, we have observed that the ensuing deformation can translate back and forth along the backbone in a manner that resembles the propagation of Davydov's Amide I soliton. Accordingly, the low-energy landscape of Myc is degenerate, and there is at least a two-state structure between which Myc oscillates at room temperature. The oscillatory behavior is in line with the expected character of Myc as an intrinsically unstructured protein.

ACKNOWLEDGMENTS

This research was supported in part by the Bulgarian Science Fund (Grant No. DNTS-CN 01/9/2014) and the China-Bulgaria Intergovernmental S&T Cooperation Project at Ministry of Science and Technology of P.R. China (2014-3). A.J.N. acknowledges support from Vetenskapsrådet, Carl Trygger's Stiftelse för vetenskaplig forskning, and a Qian Ren Grant at Beijing Institute of Technology.

-
- [1] D. C. Rapaport, *The Art of Molecular Dynamics Simulation* (Cambridge University Press, Cambridge, 2004).
 - [2] H. Gelman and M. Gruebele, *Q. Rev. Biophys.* **47**, 95 (2014).
 - [3] D. E. Shaw *et al.*, *Commun. ACM* **51**, 91 (2008).
 - [4] D. E. Shaw *et al.*, *High Performance Computing Networking, Storage and Analysis, Proceedings of the Conference* (IEEE, Los Alamitos, 2009).
 - [5] P. A. Jennings and P. E. Wright, *Science* **262**, 892 (1993).
 - [6] A. Raval, S. Piana, M. P. Eastwood, R. O. Dror, and D. E. Shaw, *Proteins* **80**, 2071 (2012).
 - [7] M. G. Saunders and G. A. Voth, *Ann. Rev. Biophys.* **42**, 73 (2013).
 - [8] M. Cascella and S. Vanni, *Chem. Mod.* **12**, 1 (2015).
 - [9] N. Goldenfeld, *Lectures on Phase Transitions and the Renormalization Group* (Addison-Wesley, Reading, MA, 1992).
 - [10] U. H. Danielsson, M. Lundgren, and A. J. Niemi, *Phys. Rev. E* **82**, 021910 (2010).
 - [11] M. Chernodub, S. Hu, and A. J. Niemi, *Phys. Rev. E* **82**, 011916 (2010).
 - [12] N. Molkenhain, S. Hu, and A. J. Niemi, *Phys. Rev. Lett.* **106**, 078102 (2011).
 - [13] A. Krokhotin, M. Lundgren, and A. J. Niemi, *Phys. Rev. E* **86**, 021923 (2012).
 - [14] A. Krokhotin, A. Liwo, A. J. Niemi, and H. A. Scheraga, *J. Chem. Phys.* **137**, 035101 (2012).

- [15] A. Krokhotin, A. Liwo, G. G. Maisuradze, A. J. Niemi, and H. A. Scheraga, *J. Chem. Phys.* **140**, 025101 (2014).
- [16] A. K. Sieradzan, A. J. Niemi, and X. Peng, *Phys. Rev. E* **90**, 062717 (2014).
- [17] A. J. Niemi, *Theor. Math. Phys.* **181**, 1235 (2014).
- [18] A. J. Niemi, in *Topological Aspects of Condensed Matter Physics*, Lecture Notes of the Les Houches Summer School 2014, edited by C. Chamon, M. Goerbig, R. Moessner, and L. Cugliandolo (Oxford University Press, Oxford, 2017).
- [19] H. Berman, J. Westbrook, Z. Feng, G. Gilliland, T. Bhat, H. Weissig, I. Shindyalov, and P. Bourne, *Nucl. Acids Res.* **28**, 235 (2000).
- [20] K. Lindorff-Larsen, S. Piana, R. O. Dror, and D. E. Shaw, *Science* **334**, 517 (2011).
- [21] R. J. Glauber, *J. Math. Phys.* **4**, 294 (1963).
- [22] B. A. Berg, *Markov Chain Monte Carlo Simulations and Their Statistical Analysis* (World Scientific, Singapore, 2004).
- [23] D. Sheiness, L. Fanshier, and J. M. Bishop, *J. Virol.* **28**, 600 (1978).
- [24] R. DePinho, K. S. Hatton, A. Tesfaye, G. D. Yancopoulos, and F. W. Alt, *Genes Dev.* **1**, 1311 (1987).
- [25] N. Meyer and L. Z. Penn, *Nat. Rev. Cancer* **8**, 976 (2008).
- [26] C. H. Arrowsmith, C. Bountra, P. V. Fish, K. Lee, and M. Schapira, *Nat. Rev. Drug Disc.* **11**, 384 (2012).
- [27] C. V. Dang, *Cell* **149**, 22 (2012).
- [28] S. K. Nair and S. K. Burley, *Cell* **112**, 193 (2003).
- [29] A. V. Follis, D. I. Hammoudeh, A. T. Daab, and S. J. Metallo, *Bioorg. Med. Chem. Lett.* **19**, 807 (2009).
- [30] B. Hess, C. Kutzner, D. van der Spoel, and E. Lindahl, *J. Chem. Theory Comput.* **4**, 435 (2008).
- [31] J. Dai, A. J. Niemi, J. He, A. Sieradzan, and N. Ilieva, *Phys. Rev. E* **93**, 032409 (2016).
- [32] A. S. Davydov, *J. Theor. Biol.* **38**, 559 (1973).
- [33] A. S. Scott, *Phys. Repts.* **217**, 1 (1992).
- [34] Please see the following <http://www.folding-protein.org>.
- [35] S. Hu, Y. Jiang, and A. J. Niemi, *Phys. Rev. D* **87**, 105011 (2013).
- [36] T. Ioannidou, Y. Jiang, and A. J. Niemi, *Phys. Rev. D* **90**, 025012 (2014).
- [37] P. L. Primalov, *Adv. Protein Chem.* **33**, 167 (1979).
- [38] P. L. Primalov, *Ann. Rev. Biophys. Biophys. Chem.* **18**, 47 (1989).
- [39] E. Shakhnovich and A. Finkelstein, *Biopolymers* **28**, 1667 (1989).
- [40] P. G. de Gennes and J. Prost, *The Physics of Liquid Crystals* (Clarendon Press, Oxford, 1995).
- [41] A. Sinelnikova, A. J. Niemi, and M. Ulybyshev, *Phys. Rev. E* **92**, 032602 (2015).
- [42] A. Krokhotin, M. Lundgren, A. J. Niemi, and X. Peng, *J. Phys.: Cond. Mat.* **25**, 325103 (2013).
- [43] M. L. Scalley and D. Baker, *Proc. Natl. Acad. Sci USA* **94**, 10636 (1997).
- [44] P. Rotkiewicz and J. Skolnick, *J. Comp. Chem.* **29**, 1460 (2008).
- [45] S. Hu, M. Lundgren, and A. J. Niemi, *Phys. Rev. E* **83**, 061908 (2011).
- [46] J. Dai, A. J. Niemi, and J. He, *J. Chem. Phys.* **145**, 045103 (2016).